Dual targeting of higher-order DNA structures by azacryptands induces DNA junction-mediated DNA damage in cancer cells

Joanna Zell, Katerina Duskova, Leïla Chouh, Madeleine Bossaert, Nicolas Chéron, Anton Granzhan, Sébastien Britton, David Monchaud

Published online 22 September 2021

Nucleic Acids Research, 2021, Vol. 49, No. 18 ***10275–10288***
https://doi.org/10.1093/nar/gkab796

Dual targeting of higher-order DNA structures by azacryptands induces DNA junction-mediated DNA damage in cancer cells

Joanna Zell[1], Katerina Duskova[1], Leïla Chouh[2,3], Madeleine Bossaert[4], Nicolas Chéron[5], Anton Granzhan[2,3], Sébastien Britton[4,*] and David Monchaud[1,*]

[1]Institut de Chimie Moléculaire de l'Université de Bourgogne (ICMUB), CNRS UMR 6302, UBFC Dijon, 21078 Dijon, France, [2]Institut Curie, CNRS UMR 9187, INSERM U1196, PSL Research University, 91405 Orsay, France, [3]Université Paris Saclay, CNRS UMR 9187, INSERM U1196, 91405 Orsay, France, [4]Institut de Pharmacologie et de Biologie Structurale (IPBS), CNRS UMR 5089, Université de Toulouse, UPS, Équipe labellisée la Ligue Contre le Cancer, 31077 Toulouse, France and [5]Pasteur, Département de chimie, École Normale Supérieure (ENS), CNRS UMR8640, PSL Research University, Sorbonne Université, 75005 Paris, France

Received April 27, 2021; Revised August 16, 2021; Editorial Decision August 31, 2021; Accepted September 01, 2021

ABSTRACT

DNA is intrinsically dynamic and folds transiently into alternative higher-order structures such as G-quadruplexes (G4s) and three-way DNA junctions (TWJs). G4s and TWJs can be stabilised by small molecules (ligands) that have high chemotherapeutic potential, either as standalone DNA damaging agents or combined in synthetic lethality strategies. While previous approaches have claimed to use ligands that specifically target either G4s or TWJs, we report here on a new approach in which ligands targeting both TWJs and G4s *in vitro* demonstrate cellular effects distinct from that of G4 ligands, and attributable to TWJ targeting. The DNA binding modes of these new, dual TWJ-/G4-ligands were studied by a panel of *in vitro* methods and theoretical simulations, and their cellular properties by extensive cell-based assays. We show here that cytotoxic activity of TWJ-/G4-ligands is mitigated by the DNA damage response (DDR) and DNA topoisomerase 2 (TOP2), making them different from typical G4-ligands, and implying a pivotal role of TWJs in cells. We designed and used a clickable ligand, TrisNP-α, to provide unique insights into the TWJ landscape in cells and its modulation upon co-treatments. This wealth of data was exploited to design an efficient synthetic lethality strategy combining dual ligands with clinically relevant DDR inhibitors.

GRAPHICAL ABSTRACT

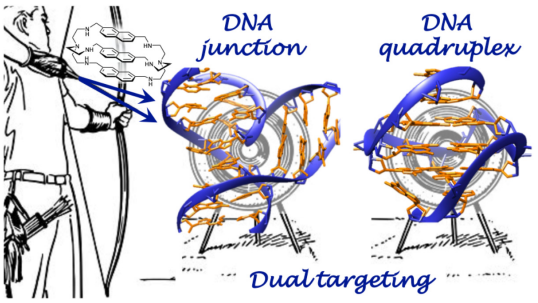

INTRODUCTION

DNA is constantly damaged by exogeneous and endogenous processes. Lesions, such as modifications and loss of bases or replication errors, interfer with DNA transactions (i.e. replication and transcription) and induce DNA damage signalling and single- (SSB) and double-strand breaks (DSB) (1–3). A complex mechanism, known as the DNA damage response (DDR), exists in higher organisms to sense damage, block the cell cycle and repair DNA lesions *via* a large variety of mechanisms. DSBs are the most dangerous and deleterious of all lesions, and two major pathways exist to repair them: homologous recombination (HR) and non-homologous end joining (NHEJ) (4–5). HR relies on a homologous template for repair, is mediated by a large number of proteins, including RAD51, and is stimulated by the activation of two kinases, namely ATM (ataxia telangiectasia mutated) kinase at DSBs, and ATR (ATM and Rad3-related) kinase at stalled replication forks. NHEJ consists in the direct ligation of the two DNA ends, and is mediated by the DNA-dependent protein kinase (DNA-PK) and

*To whom correspondence should be addressed. Tel: +33 380 399 043; Fax : +33 380 396 098; Email: david.monchaud@u-bourgogne.fr
Correspondence may also be addressed to Sébastien Britton. Tel: +33 561 175 936; Fax: +33 561 175 933; Email: sebastien.britton@ipbs.fr

DNA ligase IV-XRCC4 complexes. Prolonged DNA damage signalling induces senescence or programmed cell death (4–6).

Cancer cells are commonly deficient in DDR pathways, which can be seen as a therapeutic advantage to exploit in the fight against cancer cell proliferation (1,7). Classic chemotherapy and radiotherapy function by inducing DNA damage (3,8), which is particularly lethal in fast dividing cells with impaired DDR machinery. More recently developed treatments have improved specificity by exploiting *synthetic lethal* interactions between the inactivation of different DNA repair mechanisms: while the inactivation of a single DNA repair mechanism is tolerated *via* use of a second compensatory mechanism, the concomitant inactivation of the two mechanisms is synthetic lethal. Based on cancer's biomarkers, specific DDR deficiencies can be identified and treated by inhibitors targeting the compensatory mechanisms which are necessary for cancer cell survival (9–10).

An alternative to creating DNA damage with broad-spectrum agents, such as DNA-alkylating chemicals, ionising radiation and radiomimetics, is to create structure-specific DNA damage. Indeed, DNA is no longer seen as a rigid double helix: mounting evidence indicates that it behaves as a highly dynamic biopolymer (11–15), folding into alternative (i.e. non-B helical) DNA structures, including left-handed Z-DNA (16–17), triplex DNA (18), R-loops (19–21) and point structures such as G-quadruplexes (G4s) (22–25), i-motifs (26), three-way junctions (TWJ, or slipped loops or hairpins) (13) and four-way junctions (FWJ, or cruciform DNA or Holliday junctions) (13,27). Secondary structures are most likely transient and have a higher tendency to form during DNA transactions when the chromatin structure is open, the two strands are separated and torsional stress twists the DNA. G4s are the most studied higher-order structures for their possible regulatory roles in gene expression and replication origins (28–29). Besides these useful roles, excessive or prolonged formation of alternative structures is also correlated to replication stress (30–32), and non-B structure-forming sequences are enriched at mutation sites in cancer genomes (33). For example, TWJ- and FWJ-forming sequences are more concentrated at replication fork stall sites in various cell types in independent studies (34–36). DNA structures are known to impede DNA transactions *in vitro*, acting as roadblocks that cannot be bypassed efficiently by DNA-associated enzymes (27,37) and represent a window of opportunity to create DNA damage by using *ad hoc* ligands (3).

Numerous G4-interacting small molecules (G4 ligands (38), Figure 1A) have been shown to induce DNA damage and replicative stress signalling (39–40), in several cases at telomeres (41–44), and have shown promising therapeutic properties in synthetic lethality strategies when used in DDR-deficient systems (40,42,45–47) and in combination with DNA-damaging or DDR-inhibiting drugs (48–52). In contrast, DNA junction-targeting agents are far less developed in a cellular context (3,53). Hannon and co-workers first characterized a TWJ-binding supramolecular iron(II) helicate ligand (Figure 1B) (54), demonstrated its ability to impede DNA transactions *in vitro* (55) and its modest cytotoxic activity in cells (56). More recently, Vazquez and co-workers used a fluorescently labelled iron(II) helicate to label TWJs in cells (57), and Nitschke, Keyser and co-workers used a tetrahedral cage to detect mismatched DNA architectures *in vitro via* fluorescence quenching (58). We also reported on the ability of metallacages to interact with TWJs (59–60), but have chosen to focus on the pharmacologically more relevant small organic molecules, notably the azacryptand TrisPOB (*vide infra*), to study the antitumoral and DNA damage-inducing properties of TWJ ligands and their synergistic combination with DNA repair inhibitors (61).

Mergny *et al.* pioneered the study of azacryptands as ligands of higher-order DNA structures by demonstrating the ability of tris-acridine TrisA to bind to imperfect DNA hairpins that fold from trinucleotide repeats (65). Tris-naphthalene TrisNP (Figure 2A) was the first azacryptand described to bind TWJs *in vitro* (66); however, this ligand had initially been discarded from our search for highly specific TWJ ligands because of unwarranted interactions with G4s (67). In this regard, we studied TrisPOB, another azacryptand (Figure 2A), for its promising cellular properties (61). We now show that the potential concomitant targeting of two secondary DNA structures can yield real therapeutic dividends, echoing the 'multitargeting concept' by S. Neidle (38) that describes the targeting of mutiple G4 sites, here extended to multiple folded DNA structures. We thus investigated the genotoxic potential of a novel class of dual TWJ-/G4-ligands and report herein on the powerful antitumoral and synergistic properties of TrisNP upon co-treatment with DDR inhibitors in cancer models.

MATERIALS AND METHODS

FRET-melting assay

Experiments were performed in a 96-well plate (Agilent) using an Agilent Mx3005P equipped with FAM filters ($\lambda_{ex} = 492$ nm; $\lambda_{em} = 516$ nm). Experiments were performed in CacoK buffer (10 mM lithium cacodylate buffer with 10 mM KCl and 90 mM LiCl, pH 7.2) (final volume: 100 µl per well) with 0.2 µM DNA (labelled sequence F-TWJ-T and F21T) and 1 µM ligand. The microplate was centrifuged quickly (10 s) and then placed into the Mx3005P. After an initial equilibration step (25°C, 30 s), a rapid increase to 90°C is followed by a stepwise decrease (1°C every 30 s, 65 cycles) to 25°C and then a stepwise increase (1°C every 30 s, 65 cycles) to reach 90°C again, and measurements were made after each cycle. Final data were analyzed with Excel and OriginPro 9. The emission of FAM was normalized (0 to 1), and $T_{1/2}$ was defined as the temperature for which the normalized emission was 0.5; the reported $\Delta T_{1/2}$ values were means of 3 experiments. Competitive experiments were performed similarly, with labelled DNA (F-TWJ-T and F21T, 0.2 µM) in the presence of ligand (1.0 µM, 5 molar equiv.) and increasing amounts of the unlabelled competitor TWJ and TG4T (3.0 and 10.0 µM, 15 and 50 molar equiv.). F-TWJ-T: FAM-d[$^{5'}$A(CT)$_2$(TC)$_2$G-T$_6$-C-(GA)$_2$GCGAC-T$_6$-GTCGC(AG)$_2$T$^{3'}$]-TAMRA); F21T: FAM-d[$^{5'}$G$_3$(T$_2$AG$_3$)$_3$$^{3'}$]-TAMRA; TG4T: d[$^{5'}$(TG$_4$T)$^{3'}$]$_4$; TWJ: TWJ-S1 (d[$^{5'}CG_2A_2CG_2$CACTCG$^{3'}$]) + TWJ-S2 (d-[$^{5'}$CGAGTGCAGCGTG$_2$$^{3'}$]) + TWJ-S3 (d[$^{5'}C_2$ACGCTCGT$_2C_2G^{3'}$]).

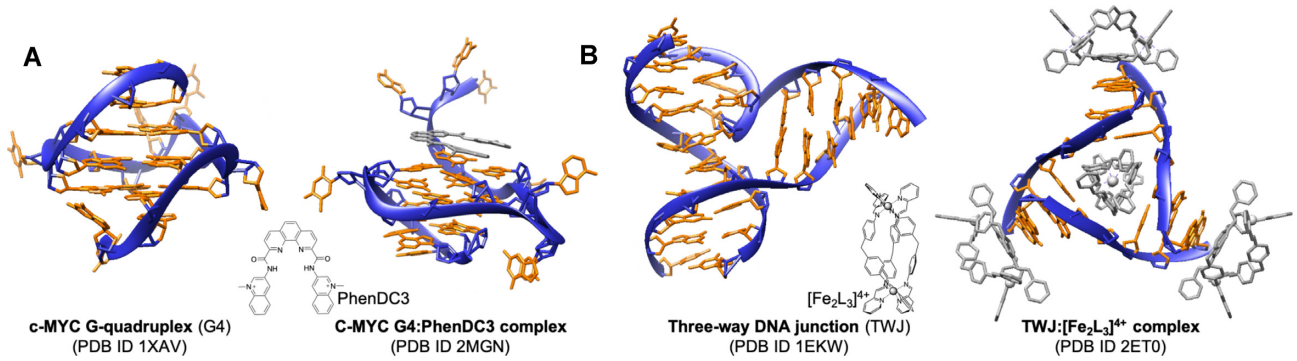

Figure 1. Crystal or NMR structures of G4-/TWJ-forming oligonucleotides without or with ligand: (**A**) G4 (62) with PhenDC3; (63) (**B**) TWJ (64) with the iron supramolecular helicate $[Fe_2L_3]^{4+}$(54).

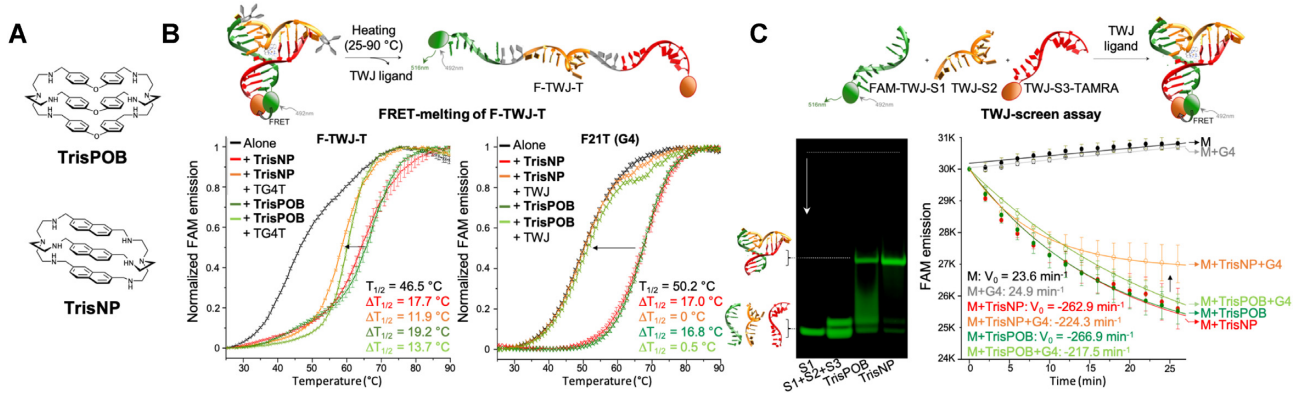

Figure 2. (**A**) Chemical structures of TrisPOB and TrisNP. (**B**) Competitive FRET-melting assays using labelled intramolecular TWJ- and G4-forming oligonucleotides: experiments performed from 25 to 90°C with F-TWJ-T (0.2 μM) in the presence of TrisNP or TrisPOB (1.0 μM, 5 mol. eq.) and competitive non-fluorescent G4 TG4T (50 mol. eq.) (left panel) and labelled G4 F21T (0.2 μM) in the presence of TrisNP or TrisPOB (1.0 μM, 5 mol. eq.) and competitive non-fluorescent TWJ (15 mol. eq.) (right panel). (**C**) TWJ-folding monitored by either PAGE (TWJ-S1 (5.0 μM), TWJ-S1 + TWJ-S2 + TWJ-S3 (M, 5.0 μM), M + TrisPOB and M + TrisNP, (5 mol. eq., 1 h; gels post-stained with SybrGold)) (left) or TWJ-Screen assays performed with a mixture of FAM-TWJ-S1, TWJ-S2 and TWJ-S3-TAMRA (M, 0.2 μM) alone or in presence of ligand (5 mol. eq.), with or without competitive TG4T (5 mol. eq.). Control experiments are provided in Supplementary Figure S1.

Polyacrylamide gel electrophoresis

Nondenaturing PAGE was performed in 15% polyacrylamide gel. Samples were prepared in 15 μl solutions of DNA or DNA/ligand mixtures. Each solution was prepared separately: TWJ-S1 alone (5 μM), [TWJ-S1 + TWJ-S2 + TWJ-S3] (or *M*) (5 μM), [*M* (5 μM) + 5 molar equiv. ligand (25 μM)]. The solutions were stirred for 1 h at 25°C during which time the gel was stacked at 7 W (5 min, 150−180 V, 43−38 mA) in TBE buffer enriched with 100 mM NaCl, pH 8.3 (68). DNA loading dye (6×, 3 μl) was added to each 15 μl solution of DNA/ligand, mixed briefly and loaded onto the gel (10 μl per well), and electrophoresis migration was performed at 7 W (<1 h). After migration, gels were stained (SYBR Gold solution, 1:10 000, 15 min, 25°C under gentle agitation) and visualized with a UVP MultiDoc-It imaging system (λ_{ex} = 302 nm).

TWJ-Screen

Experiments were performed in a 96-well format using a BMGLabtech CLARIOStar machine equipped with FAM filters (λ_{ex} = 492 nm; λ_{em} = 516 nm) at 25°C (59). Each experiment is performed in CacoK buffer (final volume: 100 μl per well), with FAM-TWJ-S1 alone (0.2 μM) and in presence of ligands (5 molar equiv.), or with mixture of FAM-TWJ-S1, TWJ-S2 and TWJ-S3-TAMRA (*M*, 0.2 μM), alone or in presence of ligand (5 molar equiv.), with or without a competitive G4 (TG4T, 5 molar equiv.). Fluorescence intensity measurements were taken every 2 min over 30 min. Initial velocity (V_0) of ligand-mediated TWJ assembly is calculated over the first 10 min of incubation.

Cell culture and cell proliferation assay

MCF7 or MDA-MB-231 cells were routinely cultured in 75 or 175 cm^2 tissue culture flasks (Nunc) at 37°C in a humidified, 5% CO_2 atmosphere in Dulbecco's modified Eagle's medium (DMEM) supplemented with 10% foetal bovine serum (FBS, Gibco) and 1% Penicillin-Streptomycin mixture (10,000 units/mL penicillin, 10,000 μg/mL streptomycin, Gibco). Cells were subcultured twice a week using standard protocols. For the cell viability assays: cells were seeded in a 96-well plate (6000 cells/well) in 160 μl of growth medium for 24 h at 37°C. Then, 40 μl of ligand solution was added to reach the final concentration of the ligands between 50 and 0.005 μM and incubated for 72 h at 37°C. The media was removed and the cells fixed with

trichloroacetic acid 10% (120 μl, 1 h at 4°C). The supernatant was removed, the fixed cells were washed 5 times with water and then dried. A solution of sulforhodamine B (SRB, 100 μl, 0.057% w/v in 1% acetic acid) was added to each well. After 30 min, the supernatant was removed and the wells were washed 3 times with 150 μl of acetic acid (1%) and dried. Tris base (150 μl, 10 mM) was added to each well and the microplate was gently shaken for 10 min at 25°C. Optical density (OD) values were determined at 530 nm. Final data were analyzed with GraphPad Prism: transforming to log concentration values, normalising (from 0 to 100; 0 for ligand-treated wells where absolute cell death was observed and 100 for ligand-untreated SRB-stained cells). LD_{50} (defined as the concentration at which 50% of the cell growth inhibition is reached) was determined by non-linear regression function for inhibition dose response. Reported LD_{50} values were means of 3 experiments. Statistics were calculated with GraphPad Prism.

Immunodetection and optical imaging protocols

MCF7 cells were seeded on glass coverslips in a 24-well plate for 24 h at 37°C. For γH2AX quantification, cells were either untreated (control) or incubated with TrisPOB and TrisNP at toxic concentrations (10× the LD_{50} determined for 72 h treatment) but for shorter times (4 h), in order to maximize the investigated effect and avoid downstream signalling such as apoptosis. For co-treatments, cells were incubated for 1 h with BNS-22 (50 μM), aphidicolin (10 μM) or DRB & BMH-21 (50 and 0.5 μM respectively), to which TrisNP (22 μM for γH2AX quantification) was added without removing the inhibitor, and incubated for a further 4 h. Cells were fixed with ice-cold PFA (2%, 15 min) and blocked with blocking buffer (1% BSA, 0.1% Triton X-100 in PBS) for 10 min at room temperature (rt). Coverslips were incubated with γH2AX antibody (1/1000 dilution in blocking buffer, EMD Millipore Corp.) for 2 h at rt in a humid dish, then cells were washed with PBS + 0.1% Triton X-100 (3 × 5 min), incubated with Alexa Fluor 647-conjugated secondary antibody (1/500 in blocking buffer, EMD Millipore Corp.) for 45 min at rt in the dark. Cells were then washed with PBS + 0.1% Triton X-100 (3 × 5 min), incubated with DAPI (10 min, 1 μg/ml in PBS) and mounted with Fluoromount. Confocal imaging was performed using a confocal laser-scanning microscope (Leica TCS SP8) with a 63× objective lens and LASX software (Leica Microsystems CMS GmbH). The samples were excited at 405 nm (DAPI) and 638 nm (Alexa Fluor 647) and the fluorescence collected at 409−499 nm (DAPI) and 649−775 nm (Alexa Fluor 647). Image processing was carried out using ImageJ and the 3D Object Counter plugin.

Click imaging

MCF7 cells were seeded on glass coverslips in a 24-well plate for 24 h at 37°C. In the case of post-fixation labelling, cells were fixed with ice cold PFA (2%, 15 min), with or without treatment with CSK buffer containing 0.7% Triton X-100 and RNase A (Sigma-Aldrich, 0.3 mg/ml) (henceforth CSK + RNAse) (2 × 3 min, rt) and treated with clickable ligand (10 μM). In the case of live cell ligand treatment, cells were either untreated (control) or incubated with TrisNP-α (3 μM, 4 h). In the case of RNAse pre-extraction, cells were treated with or without ligand, then with CSK + RNAse (5 min, rt) and fixed. For co-treatments, cells were incubated for 1 h with BNS-22 (50 μM), aphidicolin (10 μM) or DRB & BMH-21 (100/1 μM), to which TrisNP-α was added without removing the inhibitor, and incubated for a further 4 h. For AAV pre-treatment, cells were seeded with AAV1-mCherry (Vector Biolabs, #7103) (multiplicity of infection (MOI): 75000) and allowed to attach overnight, washed with DMEM, and incubated with TrisNP-α (3 μM, 4 h). Cells were then fixed with ice cold PFA (2%, 15 min), washed 3 times with PBS, and click staining was carried out with Alexa Fluor 594-azide (or Alexa Fluor 488-azide in experiments with AAV1-mCherry) (1 μM) in PBS enriched with 0.05% IGEPAL CA-630, 1 mM $CuSO_4$ and 10 mM sodium ascorbate for 30 min, followed by washing with PBS + 0.1% Triton (3 × 5 min), incubated with DAPI (10 min, 1.5 μg/ml in PBS) and mounted with Fluoromount. Confocal imaging was performed as described above. Image processing was carried out using ImageJ. Staining pattern was identical in MDA-MB-231 cells.

TrisNP-α and BG4 co-staining

MCF7 cells were treated with or without TrisNP-α (3 μM, 3 h), washed with PBS and pre-extracted by a 5 min incubation with CSK + RNAse at rt. Cells were washed 3 times on ice with cold PBS, fixed on ice (PFA 2% in PBS, 15 min) and washed 3 times with PBS. For TrisNP-α post-fixation labelling, cells were fixed then incubated with or without TrisNP-α (10 μM, 3 h) at rt. After PBS washing, click reaction was performed in PBS containing 0.05% IGEPAL CA-630, 4 mM $CuSO_4$, 10 mM sodium ascorbate and 1 μM Alexa Fluor 488-azide for 30 min at rt. Finally, cells were washed with PBS and blocked (1 h in 20 mM Tris–HCl pH 7.5, 150 mM NaCl, 2% BSA, 0.2% fish gelatine, 0.1% Triton-X 100), incubated overnight at 4°C with BG4 antibody (0.25 μg/ml in blocking buffer, mouse monoclonal, Absolute antibody, Ab00174-1.1), washed with PBS + 0.1% Tween-20 and incubated with secondary goat antibody Alexa Fluor 594 in blocking buffer (45 min, rt). DNA was stained with DAPI (1 μg/ml in PBS, 15 min) and mounted with Vectashield (Vector Laboratories). Images were acquired on a ZEISS Elyra 7 3D Lattice SIM super-resolution microscope with a 63× objective (PLANAPO NA 1.4, Zeiss) and dual sCMOS cameras (pco.edge). 3D-SIM reconstructions were performed using Zen Black (2.3). Imaging intensity parameters were adjusted differently between live and fixed treated cells using Zen Blue (3.3).

Flow cytometry

MCF7 cells were seeded (3×10^6 per T75 flask or 6×10^6 per T175 flask) for 24 h at 37°C. Cells were either untreated (control) or treated with 10 × LD_{50} of ligands for 4 h. Cells were trypsinised and fixed in suspension with PFA 1% for 15 min on ice. The PFA was removed by centrifugation, cells were resuspended and washed with PBS, and ice-cold EtOH was added for overnight storage at –20°C

until analysis (max. three nights). 1×10^6 fixed cells per condition were labelled as in optical imaging protocols: incubation with γH2AX antibody (1/1000) for 2 h at 25°C, rinsed twice with blocking buffer, then incubated with Alexa Fluor 647-conjugated secondary antibody (1/500) for 45 min before counterstaining with DAPI (2 μg/ml) for 30 min. Stained samples were analyzed by flow cytometry with a 3-laser LSRII (Becton Dickinson) using 633 nm excitation for Alexa Fluor 647 (670/30 BP filter) and 355 nm excitation for DAPI (450/50 BP filter). Debris were excluded from the analysis by gating a forward scatter versus side scatter plot (gating strategy in Supplementary Figure S3B). Integrated fluorescence measurements for Alexa Fluor 647 and DAPI were recorded for 10^4 single non-debris events. Data were plotted using FlowJo software, and cell aggregates and false positives were excluded.

Synthetic lethality cytotoxicity matrices

The antiproliferative properties of combinations of ligands and DNA repair inhibitors (DNA-PKi, ATMi, and RAD51i) were assessed *via* the SRB assay. Cells were seeded in a 96-well plate (6000 cells per well) in 160 μl of growth medium for 24 h at 37°C prior to addition of ligand/inhibitor solution prepared in DMEM in a fresh 96-well plate. Seven serial dilutions of the inhibitor were performed: 12–0.18 μM for NU7441 (DNA-PKi), 30–0.47 μM for KU55933 (ATMi) and 15–0.23 μM for B02 (RAD51i), before being distributed into a fresh 96-well plate to be mixed with ligand, which is diluted within the plate (40–0.04 μM for ligands TrisNP and TrisPOB), with the final column containing no ligand and the final row containing no inhibitor. Cell viability was measured after 72 h according to the SRB protocol described above. The IC_{50} (or LD_{50}) values (called Dm, for median-effect dose) were calculated for each inhibitor:ligand ratio (from 24:1 to 0.1875:1) according to the Chou and Talalay method (69–70). The IC_{50} values of inhibitors and ligands alone (IC_{50} of inhibitor = Dm1, IC_{50} of ligand = Dm2) were determined in control wells (single agent only). The contribution to Dm of each drug in the mixture ($D_{inhibitor}$ or D1, D_{ligand} or D2) was calculated for each ratio, as follows: at 24:1 inhibitor:ligand ratio, D1 = [Dm/(24 + 1)] × 24 and D2 = [Dm/(24 + 1)] × 1; at 12:1 inhibitor:ligand ratio, D1 = [Dm/(12 + 1)] × 12 and D2 = [Dm/(12 + 1)] × 1, etc. Then, isobolograms were constructed by plotting [D2/Dm2] versus [D1/Dm1] for each ratio. The combination index (CI, with CI < 1, = 1 and > 1 for synergistic, additive, and antagonistic effects, respectively) was also calculated for each ratio as follows: CI = (D1/Dm1) + (D2/Dm2).

RESULTS

Azacryptands interact with both TWJ and G4 *in vitro*, with a preference for TWJs

A battery of five *in vitro* techniques were employed to gain insights into how TrisNP and TrisPOB interact with both TWJ and G4: FRET-melting, PAGE gel, TWJ-Screen, ESI-MS and equilibrium dialysis. FRET-melting investigations were performed with both labelled F-TWJ-T (66) and G4-forming labelled human telomere sequence F21T (71) (Figure 2B and Supplementary Figure S1). This assay conveniently quantifies apparent TWJ- or G4-affinity by the change in the mid-transition temperature ($\Delta T_{1/2}$, °C) of fluorophore-labelled TWJ- and G4-forming oligonucleotides. TrisNP and TrisPOB induce a large and comparable stabilisation effect on both TWJ- and G4-forming oligonucleotides, with $\Delta T_{1/2} = 17.7$ and 19.2°C for F-TWJ-T, and 17.0 and 16.8°C for F21T, for TrisNP and TrisPOB, respectively. Next, competition experiments with an excess of non-labelled competitor oligonucleotide (15 and 50 molar equiv. with respect to the labelled oligonucleotide) were performed to assess the structural preferences of azacryptands. When a G4 competitor (TG4T, selected as a highly thermally stable G4 with $T_{1/2} = 85$°C) (72) was added to a F-TWJ-T/azacryptand system, the ligand-induced stabilization of F-TWJ-T was maintained to a large extent ($\Delta T_{1/2} = 11.9$ and 13.7°C for TrisNP and TrisPOB in the presence of 50 molar equiv. TG4T). Conversely, when non-labelled TWJ (15 mol. equiv.) was added as a competitor to the F21T/azacryptand system, the stabilisation of the G4 structure was totally lost ($\Delta T_{1/2} = 0$ and 0.5°C for TrisNP and TrisPOB, respectively). This shows that azacryptands interact with both G4 and TWJs, with a strong preference for TWJs.

This was further assessed by complementary isothermal assays. First, polyacrylamide gel electrophoresis (PAGE) (Figure 2C) (60–61,66), which provides a qualitative demonstration of the ability of azacryptands to readily assemble a trimolecular TWJ from the three separate strands (TWJ-S1, TWJ-S2 and TWJ-S3). Second, the TWJ-Screen assay (59–61), which quantifies the TWJ-folding ability of each ligand at a constant temperature (25°C), relies on a trimolecular system of fluorophore-labelled oligonucleotides capable of forming a TWJ structure (Figure 2C). In initial conditions, the three strands remain separate, thus a maximum fluorescence signal is observed, and upon addition of a TWJ-stabilising ligand, the TWJ structure assembles and FRET quenching reduces the fluorescent signal. The speed of TWJ-assembly promoted by the ligand is quantified by the initial velocity (V_0, min^{-1}) of the TWJ-folding-mediated FAM quenching. Both TrisNP and TrisPOB accelerate TWJ folding ($V_0 = -262.9$ and -266.9 min^{-1}, respectively) compared to ligand-free conditions in which there is no spontaneous folding of the three-strand mixture (FAM-TWJ-S1, TWJ-S2 and TWJ-S3-TAMRA, or *M* (mixture), $V_0 = 23.6$ min^{-1}, Figure 2C). Controls were performed to show that no non-specific interactions are observed between the ligand and the FAM label (ligand + TWJ-S1, $V_0 = 70.0$ and 17.4 min^{-1}, for TrisNP and TrisPOB, respectively, Supplementary Figure S1G). When performed in a competitive manner, that is, in the presence of the unlabelled TG4T, this ligand-induced TWJ assembly is marginally affected for both ligands ($V_0 = -224.3$ versus -262.9 min^{-1} for TrisNP, $V_0 = -217.5$ versus -266.9 min^{-1} for TrisPOB (Figure 2C); control: 24.9 versus 23.6 min^{-1} for *M* in absence and presence of TG4T, Supplementary Figure S1G). These results are in line with those obtained in competitive FRET-melting, demonstrating again that azacryptands do interact with both G4 and TWJs, but with a preferential affinity for TWJs.

The high TWJ affinity of TrisNP for TWJ was also shown by electrospray mass spectrometry (ESI-MS) performed with equimolar (10 μM) mixtures of TrisNP with either TWJ, G4 (TG5T) or dsDNA (ds17) (Supplementary Figure S2A–C). The spectra collected demonstrated the exclusive formation of the 1:1 TrisNP/TWJ complex, and no 2:1 TrisNP/TWJ complex is observed even when 20 μM of ligand is used. The peak of unbound TWJ–DNA is negligible, whilst the bound TrisNP/dsDNA complex is undetectable, and partial formation of the TrisNP/G4 complex is observable in identical experimental conditions. Thus for TWJ and dsDNA, the apparent equilibrium constant (K_{app}) could not be reliably calculated; only the K_{app} of the TrisNP/G4 complex could be determined (1.0×10^4 M^{-1}). To address this issue, we performed competitive equilibrium dialysis assay according to previously described protocols (61,73). This isothermal, solution-phase assay compares the affinity of a ligand for several oligonucleotide structures, each isolated within a separate dialysis chamber suspended in a solution of diffusible ligand. After 24 h of equilibration, the quantity of ligand bound to each DNA structure was quantified by exploiting the fluorescence of the azacryptands, and relative concentrations of free and bound ligands are used to determine the apparent affinity constant (Supplementary Figure S2D). K_{app} values for TrisNP and TrisPOB were high for TWJ (5.1×10^6 and 9.6×10^6 M^{-1}), at least one order of magnitude lower for G4-DNA (human telomeric sequence 22AG, 7.6×10^4 and 1.2×10^5 M^{-1}), and two orders of magnitude lower for duplex-DNA (ds17, 2.1×10^4 and 2.8×10^4 M^{-1} respectively). These results further confirm that both azacryptands bind strongly to TWJs and G4s *in vitro* with a marked preference for TWJs.

Insights into how TrisNP and TrisPOB interact with TWJs

While structural data are now widely available for a number of small molecules interacting with G4s (notably *via* NMR and X-ray crystallography studies) (74–75), little is known about how ligands bind to TWJ, with the notable exception of the solid-state investigations performed by Hannon *et al.* (*vide supra*) (54). We thus investigated how TrisPOB and TrisNP interact with TWJs *via* molecular dynamics (MD) simulations. After optimisation of TrisPOB and TrisNP conformations (Gypsum-DL, see Supplementary Data for details) (76), the ligands were docked in a TWJ structure (built from PDB: 2ET0) (54) using AutoDock 4.2 (77) and 2 μs molecular dynamics simulations were performed (Gromacs 2019.4 with the Amber99-BSC1 force field for DNA, see SI) to analyze their binding modes (78–81). The ligand-TWJ interactions were quantified by four metrics: the root-mean square deviation (RMSD), which measures the deviation of the structure throughout the simulation from the starting structure of the 2 μs simulation (i.e. the end of the equilibration); the radius of gyration (Rg); the number of hydrogen bonds between the DNA strands (H-bonds); and the solvent-accessible surface area (SASA) (Figure 3A and Supplementary Figure SI). These metrics were found to be similar for TrisNP and TrisPOB.

The second half of the simulations was clustered, and representative structures (populated at 84 and 91% of the time for TrisPOB and TrisNP, respectively) are shown in Figure 3B. The steric hindrance of both ligands induces a nucleotide base pair disruption at the cavity site, an energy penalty that is compensated by the creation of multiple π-stacking interactions. However, the way the two ligands interact with TWJ was different due to the inherent difference in structure and flexibility of the ligands: TrisPOB was found in an oblong conformation which nestles within the TWJ cavity, while TrisNP was found in a globular conformation which can even transiently form an inclusion complex (*ca.* 1% of the time) in which one isolated dT residue is sandwiched in between its naphthalene units (Figure 3B and Supplementary movies 1–4). This transient binding mode correlates with the known ability of azacyclophanes, which contain only two aromatic units, to sandwich aromatic hosts (as demonstrated by both NMR and X-ray crystallography studies) (82–84) but is more surprising for azacryptands, known to act as hosts for small anions and metal ions so far (85–87). Altogether, these findings comply with the nature of the ligands, since the diphenyl ether units give TrisPOB more flexibility due to the rotation about the C–O bonds, allowing it to adapt to, and to efficiently π-stack with the surrounding nucleobases, while the rigid naphthalene units make TrisNP prone to transiently catch isolated nucleobases in addition to π-stacking with the nucleobases that form the cavity walls.

Azacryptands are cytotoxic and induce DNA damage

The cytotoxicity of both TrisPOB and TrisNP was tested in hormone-responsive adenocarcinoma cells MCF7 (88–89), expressing oestrogen (ER), progesterone (PR) and glucocorticoid receptors (GR), and triple-negative MDA-MB-231 (90), which are ER^-, PR^- and $HER2^-$ (human epidermal growth factor receptor 2) adenocarcinoma cells, typically more aggressive. These two cell lines are routinely used to validate experimental therapeutics as they correspond to two different types of breast cancers. The median lethal dose (LD_{50}) was calculated using the Sulforhodamine B (SRB) assay (91–92) and both compounds were found quite active, with average LD_{50} values of 2.7 and 0.6 μM for TrisPOB against MCF7 and MDA-MB-231, respectively, and 5.8 and 1.6 μM for TrisNP against MCF7 and MDA-MB-231, respectively, averaged over three to six biological replicates (Supplementary Figure S3).

To prove that this cellular activity originates in the ligands' ability to trigger DNA damage, as previously described for TrisPOB (61), we assessed the induction of DNA damage through immunostaining experiments with an anti-γH2AX antibody, which reveal the phosphorylation of histone H2AX (Figure 4A, B), an established marker of DSBs (93–94). Confocal microscopy showed a significant increase in DSBs in treated cells compared to non-treated (Ctrl) cells (Figure 4A), quantified by the percentage of nuclei with >5 and >10 γH2AX foci. 75% and 71% of TrisPOB-treated and 63% and 43% of TrisNP-treated cells showed >5 and >10 foci respectively, compared to 24% and 15% in non-treated cells as an average of five or more experiments. Flow cytometry quantification also showed significant DNA damage by γH2AX immunostaining, similar to the levels previously observed for TrisPOB (Figure 4B). Results are shown as a percentage

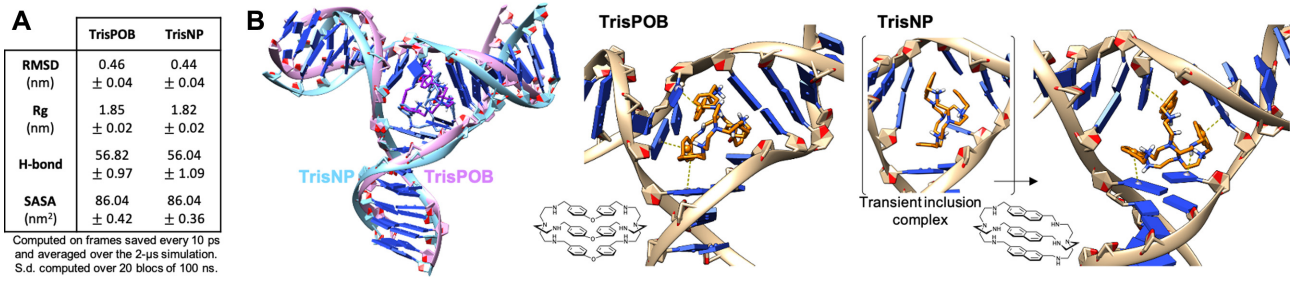

Figure 3. (**A**) Metrics quantifying the interaction between TrisPOB and TrisNP with TWJs. (**B**) Representative conformations of TrisNP and TrisPOB bound in a TWJ, obtained *via* MD simulations; π-stacking and polar–π interactions are shown as dotted lines; the transient inclusion complex in which a nucleobase (dT) is sandwiched inside TrisNP is shown in brackets.

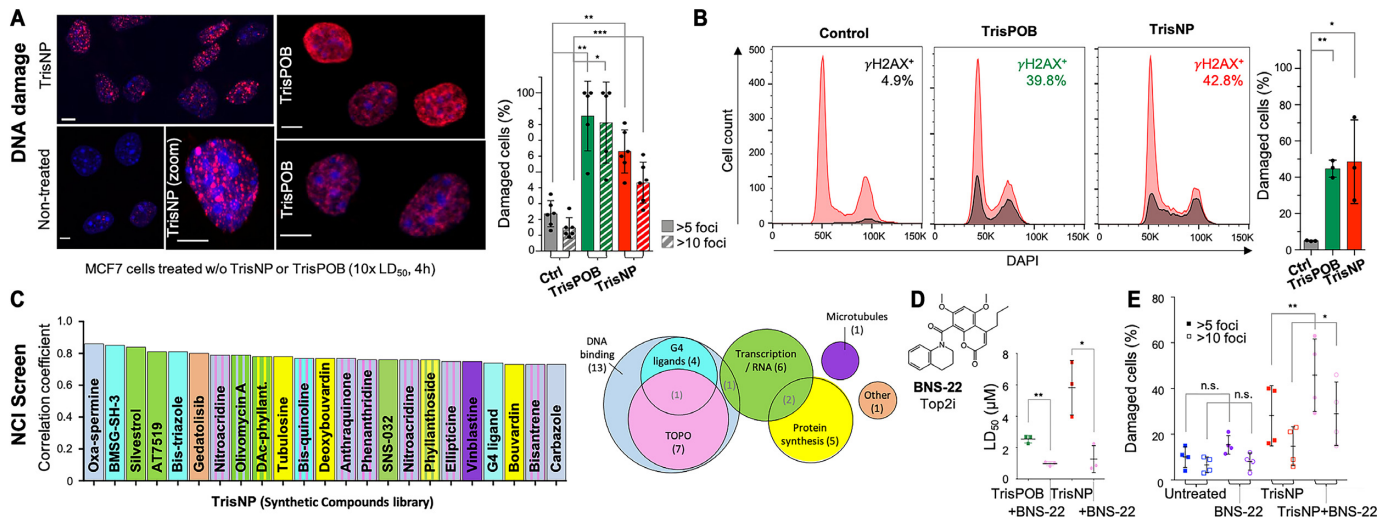

Figure 4. (**A**,**B**) Immunodetection of DNA damage in MCF7 cells non-treated or treated with 10 × LD_{50} of TrisPOB and TrisNP (9 and 22 µM) for 4 h at 37°C prior to immunolabeling with antibodies raised against γH2AX (secondary antibody labelled with Alexa Fluor 647, λ_{em} = 670 nm) and DAPI nuclear staining (λ_{em} = 450 nm); scale bars = 5 µm. γH2AX foci are quantified by fluorescence imaging (% of cells with > 5 and > 10 γH2AX foci) with ImageJ plugin 3D Object Counter (80 to 200 cells from >8 different images per condition (**A**), or quantified by flow cytometry and data treatment using FlowJo software (**B**), repeated in at least three separate experiments. (**C**) NCI databases of Synthetic Compounds (left panel and Venn diagram) tested in the NCI-60 cytotoxicity assay show the compounds with the highest correlations of cytotoxicity fingerprint with TrisNP and TrisPOB. Colour-coding shows the mechanism of action described for the compounds. (**D**) Antiproliferative activity of TrisPOB and TrisNP is markedly increased in the presence of a subtoxic concentration of BNS-22 (12.5 µM) in MCF7 cells over 72 h. (**E**) Immunodetection of DNA damage in MCF7 cells treated with or without BNS-22 (50 µM, 5 h) and/or 10 × LD_{50} of TrisNP (4 h) prior to immunolabeling with γH2AX-specific antibody. Quantified as previously. *P* values were calculated using a paired, two-tailed *t* test. ns: $P > 0.05$; $*P < 0.05$; $**P < 0.005$; **P < 0.0005 (**A**, **B**, **D**, **E**).

of γH2AX-stained cells (an average of 45% (TrisPOB) and 49% (TrisNP) of cells when gating is performed to assign 5% of non-treated cells as γH2AX-positive ($n = 3$). No significant difference in cell cycle was observed (Supplementary Figure S3C).

To further investigate the mechanism of the antiproliferative activity of TrisNP and TrisPOB, the compounds were submitted to the USA National Cancer Institute's (NCI) NCI-60 Human Tumor Cell Lines Screen. In this screen, the cytotoxicity fingerprint of novel compounds obtained in 60 well-established tumour cell lines is compared with that of known, previously tested compounds using the COMPARE algorithm, in order to put forward mechanistic hypotheses (95–96). The cytotoxicity patterns of TrisNP and TrisPOB (NSC 818603 and NSC 818604, respectively) were compared with the molecules in two chemical libraries: the Synthetic Compounds library, the largest and most varied (400 compounds) and the Marketed Drugs library, which contains the drugs with the best studied mechanisms (90 compounds, Figure 4C and Supplementary Figure S3). In both libraries, the highest correlation coefficients were obtained with DNA-binding compounds, including several G4 ligands (e.g. the naphthalene diimide BMSG-SH-3 developed as a pancreatic cancer drug (97) and bis-triazole G4 ligands) (98). Topoisomerase (TOP) inhibitors, e.g. phenanthridinium derivatives (99), were also found to rank highly. A full list of correlated drugs and proposed mechanisms is available in the Supplementary Data. These findings are in line with recent genetic screens indicating that ligands targeting higher-order DNA structures, such as pyridostatin (PDS) and CX-5461, exert at least a part of their toxicity *via* G4-mediated TOP2 trapping (100–102), which ultimately triggers DNA damage (3,39). This series of results thus indicates that the toxicity signatures of both

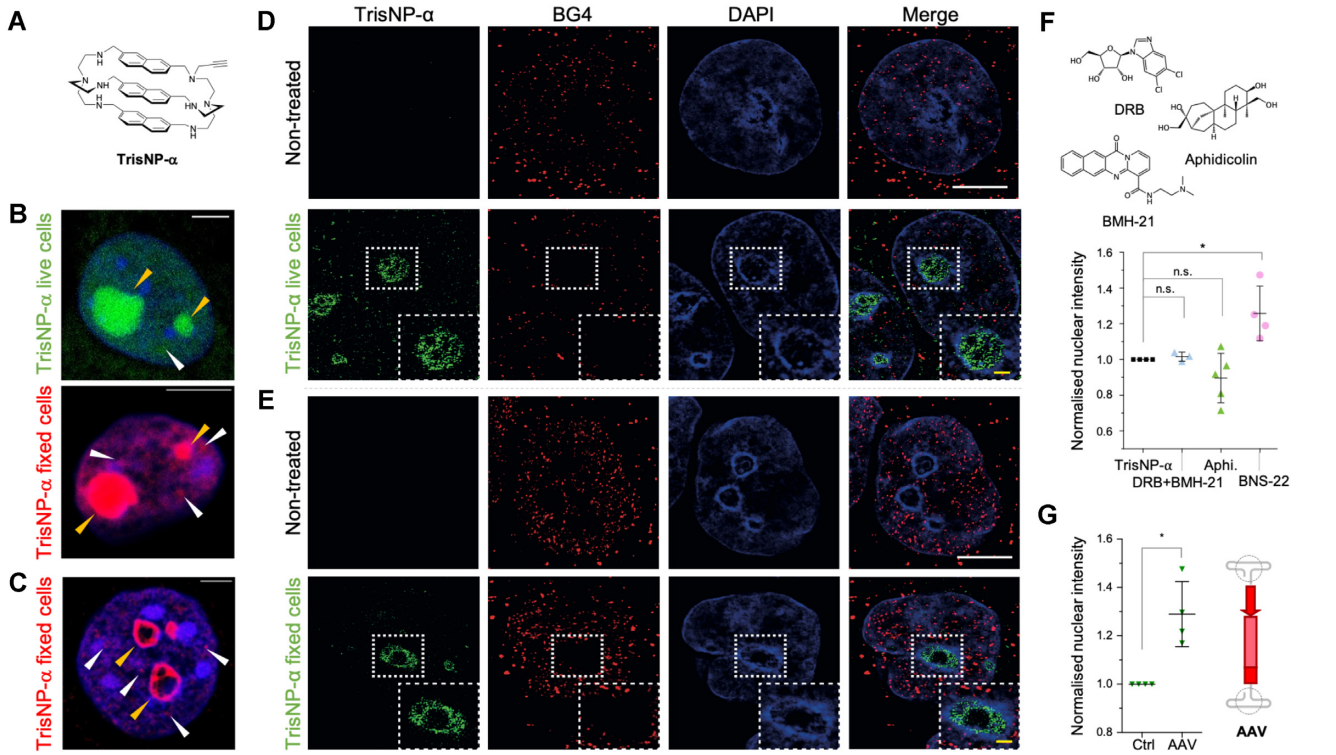

Figure 5. (**A**) Structure of TrisNP-α. (**B,C**) *In situ* click imaging obtained with TrisNP-α (3 μM, 4 h) incubated in live or fixed cells, then illuminated with Alexa Fluor 488-azide (green, live cell incubation) or Alexa Fluor 594-azide (red, post-fixation incubation). Ligand is present in the nucleoli (yellow arrows) and the nucleoplasm (white arrows). Cells pre-extracted (**C**) with CSK + RNAse show perinucleolar staining (yellow arrows). Nuclei are counterstained with DAPI (blue). Scale bars = 5 μm. (**D**, **E**) Super-resolution images of MCF7 cells are treated with TrisNP-α (3 h, 3 μM), pre-extracted with CSK + RNase A, fixed, clicked, and co-stained with BG4 antibody (**D**) or pre-extracted with CSK + RNase A, fixed, incubated with TrisNP-α (3 h, 10 μM), clicked and co-stained with BG4 antibody (**E**). Nuclei are counterstained with DAPI. White scale bar = 5 μm, yellow scale bar = 1 μm. (**F**) Change in nuclear intensity of live TrisNP-α click staining after pre-treatment with inhibitors DRB + BMH-21 (100/1 μM), aphidicolin (10 μM) and BNS-22 (50 μM). (**G**) TrisNP-α nuclear intensity increases with AAV1-mCherry treatment, stained as previously described and labelled after fixation *via* click reactions with AF488-azide. Nuclear intensity after inhibitor or AAV treatment was quantified in FIJI ImageJ and normalised to TrisNP-α staining. *P* values were calculated using a paired, two-tailed *t* test. ns: $P > 0.05$; $^*P < 0.05$ (**F**, **G**).

TrisNP and TrisPOB resemble those of strong antiproliferative agents, which mostly act through DNA binding, with a particular ability to interact with higher-order DNA structures, and might induce topoisomerase-mediated DNA damage.

Mechanistic studies of dual ligands with topoisomerase inhibition

Following the indications from the NCI60 data that topoisomerases may be involved in cytotoxicity, we tested the effect of co-treatment with a catalytic TOP2 inhibitor BNS-22 (103). TOP2 inhibitors are categorized into two families: the most used family is the TOP2 poisons, which stabilize the covalently bound TOP2 enzyme-DNA cleaving complex (TOP2cc), and lead to DSBs; the second family is the TOP2 catalytic inhibitors, which are able to rescue the DNA damaging effects of TOP2 poisons (104). BNS-22 efficiently suppressed cytotoxicity and γH2AX induction of the TOP2 poison etoposide (Supplementary Figure S4A) in MCF7 cells, indicating that it efficiently functions as a catalytic TOP2 inhibitor in MCF7 cells. While inhibition of TOP2 has been described to block the cytotoxic activity of G4 ligands (102), it had the opposite effect on TrisNP by repeatably reducing its LD_{50} by a factor of *ca*. 4.5, from an average of 5.8 to 1.3 μM (Figure 4D) when BNS-22 is used at a single non-toxic concentration. Similar effects were observed with TrisPOB (from 2.54 to 0.98, a 2.6-fold decrease). DNA damage induction was quantified *via* γH2AX immunostaining, proving to be significantly increased when cells were co-treated with TrisNP and BNS-22, compared to TrisNP alone (Figure 4E), whilst BNS-22 alone at this concentration induces a negligible amount of DNA damage. No effect was observed on co-treatment with etoposide, but the latter had little cytotoxicity in MCF7 cells at all (Supplementary Figure S4A). The synergic relationship between TrisNP and BNS-22 is thus opposite to what was reported for PDS (102), indicating that azacryptands act through a distinct mechanism of action than a known G4 ligand, which reinforces our hypothesis regarding preferential TWJ targeting in cells. This effect could originate in the higher prevalence of TWJ-forming motifs compared to G4-forming motifs, as there are approximately 3-fold more direct repeat sequences in the human genome than G4-forming sequences (33), and *ca*. 50% of the genome is made up of repetitive sequences (105).

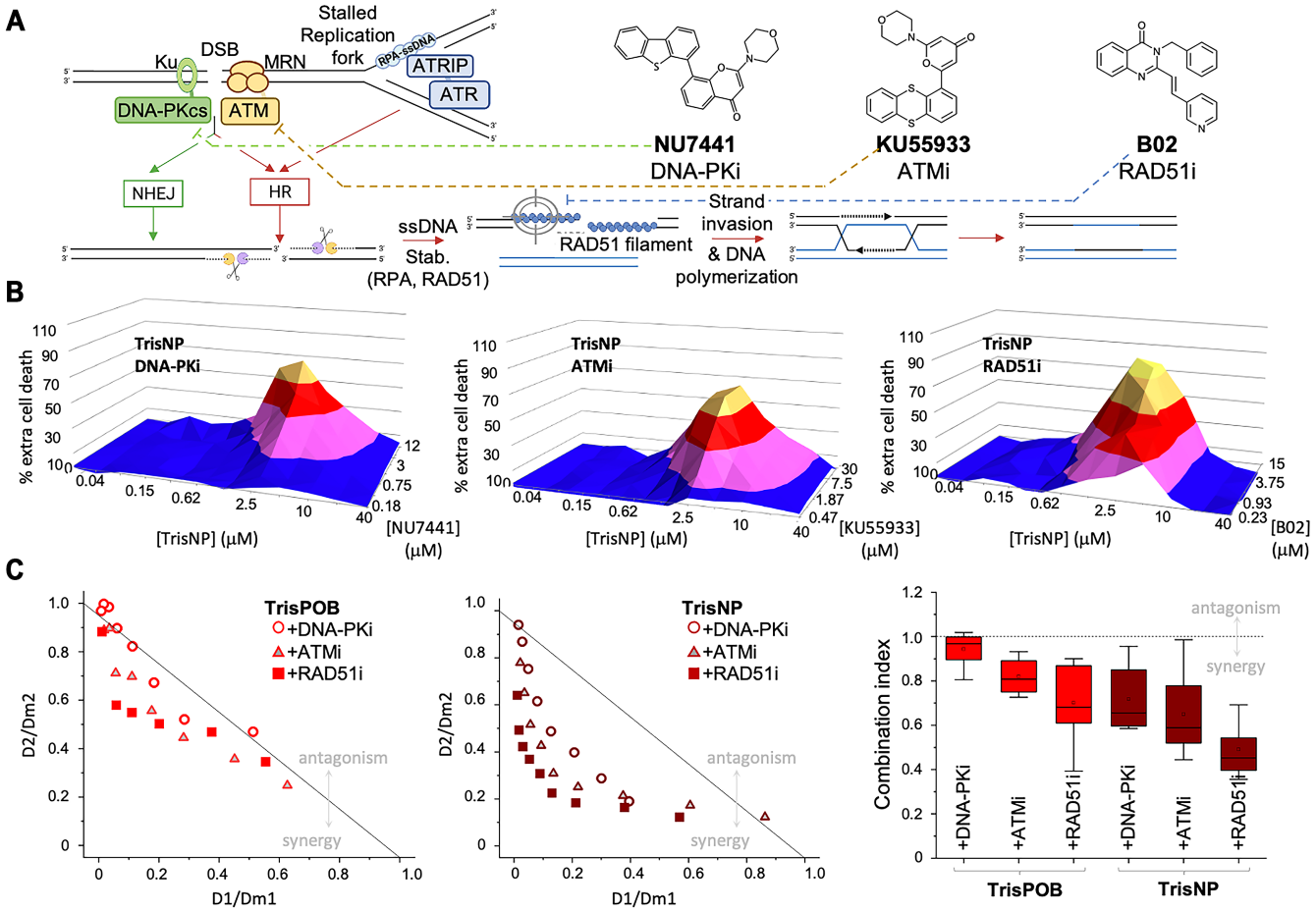

Figure 6. (**A**) Double-strand breaks (DSB) and stalled replication forks are repaired by HR and NHEJ, mediated by DNA-PK and ATM kinases and RAD51. Created with BioRender. Chemical structure of DDR inhibitors NU7441 (DNA-PKi), KU55933 (ATMi) and B02 (RAD51i). (**B**) 3D pyramid plots showing the percentage of extra cell death for the combination of TrisNP (lethal concentration range: 0–40 μM), with DNA-PKi, ATMi, or RAD51i (non-lethal concentration range, see Supplementary Data). Results are the average of three separate experiments each containing technical duplicates. (**C**) Normalised isobolograms for combination of TrisPOB or TrisNP with DNA-PKi (circles), ATMi (triangles), and RAD51i (squares). Points above the grey horizontal line show antagonism between agents, below the line show synergism. Combination index graph (right) of the same co-treatments. Derived from the same raw data as the pyramid plots in Figure 5B.

Traceable TrisNP analogue localizes in nucleoli and nucleoplasm

To further investigate this, an analogue of TrisNP with a small terminal alkyne modification (TrisNP-α, Figure 5A, see Supplementary Data for synthetic procedure) was synthesized as a chemical biology tool to quantify the accumulation of TrisNP in cells by *in situ* click imaging, and to assess the modulation of the TWJ landscape upon co-treatments (106). TrisNP-α presented *in vitro* TWJ-binding properties similar to TrisNP, albeit with a slightly lower affinity (Supplementary Figure S1E), presumably due to the steric hindrance introduced by the alkyne appendage. MCF7 cells were incubated with TrisNP-α, prior to fixation and bioorthogonal copper-catalysed alkyne-azide click reaction with an azide-tagged fluorophore, in order to localize TrisNP-α in cells (Supplementary Figure S5A). TrisNP-α localized primarily in the nucleus (nucleoplasm), and particularly in the nucleoli (yellow arrows, Figure 5B and Supplementary Figure S5B), when incubated both in live cells and in fixed cells. Nucleoplasmic *foci* were observable (white arrows) in weakly DAPI-labeled zones (euchromatin marker). The staining obtained when incubating TrisNP-α with living cells or after fixation was very similar, indicating that TWJ structures are present in cells even without being stabilised by TWJ ligands. Pre-extraction with CSK + RNase A before fixation (108) was also performed to focus on the DNA-associated staining (Figure 5C). This revealed that the inner part of the nucleolar TrisNP-α staining is lost upon RNase A treatment, indicating that this treatment efficiently removed RNA and that part of the staining observed without CSK + RNase pre-extraction is likely to correspond to RNA secondary structures. This also revealed that TrisNP-α specifically labels an RNase-resistant perinucleolar compartment partly colocalizing with the perinucleolar heterochromatin. This region around the nucleoli is likely to represent nucleolus-associated DNA domains (NADs) (109–111), which contain weakly transcribed heterochromatic regions of low gene density including centromeric and pericentromeric satellite repeats and subtelomeric regions, all of which containing palindromic and repetitive

sequences, prone to form secondary structures including TWJs (112).

We then used super-resolution 3D structured illumination microscopy (3D-SIM) to evaluate the relative patterns obtained with the TrisNP-α staining and with the G4-specific antibody BG4, which is here a recombinant IgG1 antibody in which the variable parts have been replaced by the single-chain variable fragment (scFv) of the initially described BG4 (107) (Figure 5D, E and Supplementary Figure S5C, D). CSK + RNAse A treatment was also performed to improve BG4 staining. Aside from the perinucleolar regions, small and weak TrisNP-α foci were observable dispersed in the nucleoplasm, which did not colocalize with the denser nucleoplasmic foci of BG4. Importantly, no nucleolar or perinucleolar staining was observed with BG4. Altogether these data support that TrisNP binds principally to non-BG4 labelled structures, associated to or in proximity with NADs. The lack of colocalization between the BG4 and TrisNP-α staining together with the fact that the intensity of the BG4 signal is not modified by the incubation of living cells with TrisNP-α, support the notion that TrisNP-α preferentially targets DNA junctions in cells.

TrisNP-α staining is modulated by inhibitors of DNA transactions and exogenous TWJs

BNS-22 pre-treatment was found to increase the intensity of TrisNP-α staining, indicating that TWJs become more prevalent upon TOP2 inhibition (Figure 5F). This presents a novel tool to study dynamic DNA mechanisms, and corresponds to the role of topoisomerases in reducing helical strain in DNA (113), thus reducing the formation of alternative DNA structures (114–115). More specifically, TOP2 is described not only to release DNA supercoiling, but also to recognise DNA structures (116–117) and induce DSB formation at these sites (118–119). TOP2 poisons are frequently included in first and second line anticancer therapies (120–121), and cancer cells can develop resistance by multiple mechanisms including through reduced TOP2 activity (122). Altogether, our results imply that azacryptands could prove useful to treat cancers that have developed resistance to TOP2 poisons, since azacryptand treatment could confer a greater sensitivity to these molecules through increased levels of stabilized TWJs.

We also investigated if certain DNA transactions are more favourable to TWJ formation. Cells were pre-treated with either transcription inhibitors (BMH-21 (123) and 5,6-dichloro-1-β-D-ribofuranosylbenzimidazole (DRB) (124), which inhibit RNA polymerases I and II, respectively) or replication inhibitor aphidicolin (Aphi, Figure 5F) (125). Inhibitor concentrations were optimized for efficient inhibition of transcription/replication using clickable nucleotides EdU and EU (Supplementary Figure S6A, B). Using these conditions, we found that transcription inhibition with DRB/BMH-21 had no effect on TrisNP-α click staining intensity, whilst replication inhibition with Aphi reduced TrisNP-α staining, albeit in a variable and non-statistically significant manner, indicating that TWJ-formation might be preferentially dependent on replication rather than transcription. This could not be confirmed by monitoring TrisNP-induced γH2AX signalling, since no significant change in γH2AX staining by transcription/replication inhibition was observed, whilst transcription inhibition alone induced important amounts of damage signalling (Supplementary Figure S6A). Again, these results are in contrast with what was described for PDS, where Aphi and DRB pre-treatments were found to reduce PDS-induced γH2AX signalling (39). This indicates that G4 formation is linked to these two major DNA transactions, whereas TWJ formation may be more specific to replication, and more difficult to disrupt once stabilized by *ad hoc* ligands. Direct comparison with PDS was hindered by the non-toxicity of PDS and other G4-ligands in MCF7 cells ($LD_{50} > 100$ μM, Supplementary Figure S6C).

To further demonstrate that TrisNP-α targets TWJs in a cellular context, we employed a common viral gene vector, the adeno-associated virus (AAV) (126), which contains a TWJ in each of its two inverted terminal repeats (ITRs, the only part of the genome required for AAV uptake) (Figure 5G) (127). AAV is quickly taken up into cells and transcribed. We first verified that MCF7 cells could take up AAV1-mCherry (henceforth AAV1) and express mCherry by fluorescence microscopy. Next, we incubated MCF7 cells with TrisNP-α and monitored the ligand/ITRs interaction by click chemistry. As seen in Figure 5G, TrisNP-α staining increased significantly on AAV1 incorporation (1.3-fold averaged over 4 biological repeats), thus providing an additional strong argument in favour of the interaction of TrisNP-α with TWJ structures in cells.

DNA junction ligands are synthetically lethal with DDR inhibitors

A strategy that has received growing interest is the development of drug combinations to provoke chemically-induced synthetic lethality, notably by co-treating cancer cells with DNA damaging agents and DDR inhibitors (3,10,46,128). DDR inhibitors targeting clinically relevant cellular processes were used (Figure 6A): NU7441, or DNA-PKi (inhibitor of DNA-PK, involved in NHEJ) (129), KU55933, or ATMi (inhibitor of ATM, involved in HR and checkpoint activation) (130) and B02, or RAD51i (inhibitor of RAD51, involved in HR) (131). Synergic effects between two cytotoxic drugs were tested by measuring the survival of cells in an 8 × 12 matrix of drug concentrations. TrisNP showed strong synergy with DDR inhibitors, as represented by the pyramid graphs (Figure 6B) where a peak, indicative of a synergic effect, shows extra cell death compared to the simple addition of cell death induced by the two drugs alone, according to the Loewe additivity model (132). Another reliable representation of the cytotoxic effects of drug combinations is provided by the combination index (CI), indicating synergistic, additive and antagonistic effects respectively when CI < 1, = 1, and > 1 (70). The synergy of TrisNP with DDR inhibitors was even stronger than what was previously reported for TrisPOB (61). TrisNP shows low, strongly synergic CI values with the three DDR inhibitors (average CI = 0.71, 0.64 and 0.49 with DNA-PKi, ATMi and RAD51i, respectively, and 0.94, 0.82 and 0.70 for TrisPOB) (Figure 6C). This implies that both NHEJ and HR pathways are implicated in the repair of azacryptand-

induced damage, and strongly supports the conclusion that TrisNP induces genotoxic DSBs.

DISCUSSION

In a continuation of our studies of the therapeutic potential of small molecules that target alternative DNA structures, we describe here a novel family of highly promising candidates, able to interact with two non-B DNA structures: three-stranded three-way DNA junctions and four-stranded G-quadruplex-DNA. These two ligands, TrisPOB and TrisNP, that belong to the family of azacryptands, display high toxicity in two cancer cell lines (MCF7 and MDA-MB-231) *via* induction of DNA damage, most notably DSBs. TrisNP and its traceable analogue TrisNP-α, the first 'clickable' probe belonging to this novel family of molecules, were used as chemical biology tools to study the formation and toxicity of ligand-stabilized DNA structures in cells, and provide mechanistic insights into the origins of their antiproliferative activity. Although further validation is required, this molecule could be seen as the first cellular probe for TWJ formation. Due to the elusive and transient nature of TWJs, currently available molecular tools are not fully suitable for their studies; however we continue searching for methods that could prove that TrisNP(-α) genuinely binds to TWJs in cells.

Interestingly, the cellular activity of these dual ligands is rather different from that of typical G4-ligands, for which the opposite response was reported for co-treatments with both TOP2 and transcription inhibitors. Azacryptands also distinguish themselves from G4-ligands by their high toxicity in MCF-7 cells, whilst benchmark G4-ligands such as PDS (39,133), PhenDC3 (134–135) and 360A (135–137) are non-toxic (LD_{50} > 100 μM, Supplementary Figure S6E). The chemotherapeutic potential of these molecules can be strongly potentiated when included in synthetic lethality combinations, demonstrated here by their highly synergic cytotoxicity profiles in combination with DDR inhibitors. Thus, azacryptands act *via* a distinct mechanism to that of G4-ligands and topoisomerase poisons, thus representing new and promising weapons in the chemical arms race with cancers, especially to treat cancers resistant to TOP2 poisons.

SUPPLEMENTARY DATA

Supplementary Data are available at NAR Online.

ACKNOWLEDGEMENTS

The authors are grateful to Anne Cucchiarini (Institut Curie) for HPLC analyses, Marc Pirrotta (ICMUB) for FRET-melting and TWJ-Screen investigations, and both the flow cytometry (Plateforme de Cytométrie de l'UMR1231) and optical imaging platforms (Plateforme Dimacell, INRA, Dijon) of the Université de Bourgogne Franche-Comté (supported by Conseil Régional de Bourgogne) and the TRI-IPBS Imaging Core Facility, member of TRI-Genotoul. Data of the NCI60 screening assay were obtained thanks to the National Cancer Institute Developmental Therapeutics Program (NCI/DTP, https://dtp.cancer.gov).

FUNDING

CNRS (to N.C., A.G., S.B., D.M.); INSERM Plan Cancer 2014–2019 [19CP117-00 for S.B. and D.M.]; Agence Nationale de la Recherche [ANR-17-CE17-0010-01 to A.G. and D.M., ANR-17-CE18-0002-01 for S.B.]; European Union [PO FEDER-FSE Bourgogne 2014/2020 programs, grant BG0021532]; HPC resources of IDRIS under the allocation 2020–077156 made by GENCI. Funding for open access charge: INSERM Plan Cancer 2014-2019 [19CP117-00].

Conflict of interest statement. None declared.

REFERENCES

1. Jackson,S.P. and Bartek,J. (2009) The DNA-damage response in human biology and disease. *Nature*, **461**, 1071–1078.
2. Ciccia,A. and Elledge,S.J. (2010) The DNA damage response: making it safe to play with knives. *Mol. Cell*, **40**, 179–204.
3. Zell,J., Rota Sperti,F., Britton,S. and Monchaud,D. (2021) DNA folds threaten genetic stability and can be leveraged for chemotherapy. *RSC Chem. Biol*, **2**, 47–76.
4. Hustedt,N. and Durocher,D. (2017) The control of DNA repair by the cell cycle. *Nat. Cell Biol*, **19**, 1–9.
5. Scully,R., Panday,A., Elango,R. and Willis,N.A. (2019) DNA double-strand break repair-pathway choice in somatic mammalian cells. *Nat. Rev. Mol. Cell Biol*, **20**, 698–714.
6. Verma,N., Franchitto,M., Zonfrilli,A., Cialfi,S., Palermo,R. and Talora,C. (2019) DNA damage stress: cui prodest? *Int. J. Mol. Sci*, **20**, 1073.
7. O'Connor,M.J. (2015) Targeting the DNA damage response in cancer. *Mol. Cell*, **60**, 547–560.
8. Swift,L.H. and Golsteyn,R.M. (2014) Genotoxic anti-cancer agents and their relationship to DNA damage, mitosis, and checkpoint adaptation in proliferating cancer cells. *Int. J. Mol. Sci*, **15**, 3403–3431.
9. Kaelin,W.G. (2005) The concept of synthetic lethality in the context of anticancer therapy. *Nat. Rev. Cancer*, **5**, 689–698.
10. O'Neil,N.J., Bailey,M.L. and Hieter,P. (2017) Synthetic lethality and cancer. *Nat. Rev. Genet*, **18**, 613–623.
11. Belotserkovskii,B.P., Mirkin,S.M. and Hanawalt,P.C. (2013) DNA sequences that interfere with transcription: implications for genome function and stability. *Chem. Rev*, **113**, 8620–8637.
12. Técher,H., Koundrioukoff,S., Nicolas,A. and Debatisse,M. (2017) The impact of replication stress on replication dynamics and DNA damage in vertebrate cells. *Nat. Rev. Genet*, **18**, 535.
13. Khristich,A.N. and Mirkin,S.M. (2020) On the wrong DNA track: Molecular mechanisms of repeat-mediated genome instability. *J. Biol. Chem*, **295**, 4134–4170.
14. Bochman,M.L., Paeschke,K. and Zakian,V.A. (2012) DNA secondary structures: stability and function of G-quadruplex structures. *Nat. Rev. Genet*, **13**, 770–780.
15. Zhao,J., Bacolla,A., Wang,G. and Vasquez,K.M. (2010) Non-B DNA structure-induced genetic instability and evolution. *Cell. Mol. Life Sci*, **67**, 43–62.
16. Rich,A. and Zhang,S. (2003) Z-DNA: the long road to biological function. *Nat. Rev. Genet*, **4**, 566.
17. Ravichandran,S., Subramani,V.K. and Kim,K.K. (2019) Z-DNA in the genome: from structure to disease. *Biophys. Rev*, **11**, 383–387.
18. Duca,M., Vekhoff,P., Oussedik,K., Halby,L. and Arimondo,P.B. (2008) The triple helix: 50 years later, the outcome. *Nucleic Acids Res.*, **36**, 5123.
19. Aguilera,A. and Gómez-González,B. (2017) DNA–RNA hybrids: the risks of DNA breakage during transcription. *Nat. Struct. Mol. Biol*, **24**, 439.

20. Santos-Pereira,J.M. and Aguilera,A. (2015) R loops: new modulators of genome dynamics and function. *Nat. Rev. Genet*, **16**, 583–597.
21. Crossley,M.P., Bocek,M. and Cimprich,K.A. (2019) R-loops as cellular regulators and genomic threats. *Mol. Cell*, **73**, 398–411.
22. Rhodes,D. and Lipps,H.J. (2015) G-quadruplexes and their regulatory roles in biology. *Nucleic Acids Res.*, **43**, 8627–8637.
23. Spiegel,J., Adhikari,S. and Balasubramanian,S. (2020) The structure and function of DNA G-quadruplexes. *Trends Chem*, **2**, 123–136.
24. Varshney,D., Spiegel,J., Zyner,K., Tannahill,D. and Balasubramanian,S. (2020) The regulation and functions of DNA and RNA G-quadruplexes. *Nat. Rev. Mol. Cell Biol*, **21**, 459–474.
25. Tian,T., Chen,Y.-Q., Wang,S.-R. and Zhou,X. (2018) G-quadruplex: a regulator of gene expression and its chemical targeting. *Chem*, **4**, 1314–1344.
26. Abou Assi,H., Garavís,M., González,C. and Damha,M.J. (2018) i-Motif DNA: structural features and significance to cell biology. *Nucleic Acids Res.*, **46**, 8038–8056.
27. Mirkin,E.V. and Mirkin,S.M. (2007) Replication fork stalling at natural impediments. *Microbiol Mol. Biol. Rev*, **71**, 13–35.
28. Valton,A.-L. and Prioleau,M.-N. (2016) G-quadruplexes in DNA replication: a problem or a necessity? *Trends Genet.*, **32**, 697–706.
29. Kim,N. (2019) The interplay between G-quadruplex and transcription. *Curr. Med. Chem*, **26**, 2898–2917.
30. Zeman,M.K. and Cimprich,K.A. (2014) Causes and consequences of replication stress. *Nat. Cell Biol*, **16**, 2.
31. Dobbelstein,M. and Sørensen,C.S. (2015) Exploiting replicative stress to treat cancer. *Nat. Rev. Drug Discov.*, **14**, 405–423.
32. Gaillard,H., García-Muse,T. and Aguilera,A. (2015) Replication stress and cancer. *Nat. Rev. Cancer*, **15**, 276.
33. Georgakopoulos-Soares,I., Morganella,S., Jain,N., Hemberg,M. and Nik-Zainal,S. (2018) Noncanonical secondary structures arising from non-B DNA motifs are determinants of mutagenesis. *Genome Res.*, **28**, 1264–1271.
34. Voineagu,I., Narayanan,V., Lobachev,K.S. and Mirkin,S.M. (2008) Replication stalling at unstable inverted repeats: interplay between DNA hairpins and fork stabilizing proteins. *Proc. Natl. Acad. Sci. U.S.A*, **105**, 9936–9941.
35. Voineagu,I., Surka,C.F., Shishkin,A.A., Krasilnikova,M.M. and Mirkin,S.M. (2009) Replisome stalling and stabilization at CGG repeats, which are responsible for chromosomal fragility. *Nat. Struct. Mol. Biol*, **16**, 226–228.
36. Shastri,N., Tsai,Y.-C., Hile,S., Jordan,D., Powell,B., Chen,J., Maloney,D., Dose,M., Lo,Y. and Anastassiadis,T. (2018) Genome-wide identification of structure-forming repeats as principal sites of fork collapse upon ATR inhibition. *Mol. Cell*, **72**, 222–238.
37. Lerner,L.K. and Sale,J.E. (2019) Replication of G quadruplex DNA. *Genes*, **10**, 95.
38. Neidle,S. (2017) Quadruplex nucleic acids as targets for anticancer therapeutics. *Nat. Rev. Chem*, **1**, 0041.
39. Rodriguez,R., Miller,K.M., Forment,J.V., Bradshaw,C.R., Nikan,M., Britton,S., Oelschlaegel,T., Xhemalce,B., Balasubramanian,S. and Jackson,S.P. (2012) Small-molecule-induced DNA damage identifies alternative DNA structures in human genes. *Nat. Chem. Biol*, **8**, 301–310.
40. Xu,H., Di Antonio,M., McKinney,S., Mathew,V., Ho,B., O'Neil,N.J., Santos,N.D., Silvester,J., Wei,V., Garcia,J. *et al.* (2017) CX-5461 is a DNA G-quadruplex stabilizer with selective lethality in BRCA1/2 deficient tumours. *Nat. Commun*, **8**, 14432.
41. Rizzo,A., Salvati,E., Porru,M., D'Angelo,C., Stevens,M.F., D'Incalci,M., Leonetti,C., Gilson,E., Zupi,G. and Biroccio,A. (2009) Stabilization of quadruplex DNA perturbs telomere replication leading to the activation of an ATR-dependent ATM signaling pathway. *Nucleic. Acids. Res.*, **37**, 5353–5364.
42. Salvati,E., Leonetti,C., Rizzo,A., Scarsella,M., Mottolese,M., Galati,R., Sperduti,I., Stevens,M.F.G., D'Incalci,M., Blasco,M. *et al.* (2007) Telomere damage induced by the G-quadruplex ligand RHPS4 has an antitumor effect. *J. Clin. Invest*, **117**, 3236–3247.
43. Pennarun,G., Granotier,C., Hoffschir,F., Mandine,E., Biard,D., Gauthier,L.R. and Boussin,F.D. (2008) Role of ATM in the telomere response to the G-quadruplex ligand 360A. *Nucleic Acids Res.*, **36**, 1741–1754.
44. Gauthier,L.R., Granotier,C., Hoffschir,F., Etienne,O., Ayouaz,A., Desmaze,C., Mailliet,P., Biard,D.S. and Boussin,F.D. (2012) Rad51 and DNA-PKcs are involved in the generation of specific telomere aberrations induced by the quadruplex ligand 360A that impair mitotic cell progression and lead to cell death. *Cell. Mol. Life Sci*, **69**, 629–640.
45. Zimmer,J., Tacconi,E.M.C., Folio,C., Badie,S., Porru,M., Klare,K., Tumiati,M., Markkanen,E., Halder,S., Ryan,A. *et al.* (2016) Targeting BRCA1 and BRCA2 deficiencies with G-quadruplex-interacting compounds. *Mol. Cell*, **61**, 449–460.
46. McLuckie,K.I.E., Di Antonio,M., Zecchini,H., Xian,J., Caldas,C., Krippendorff,B.F., Tannahill,D., Lowe,C. and Balasubramanian,S. (2013) G-quadruplex DNA as a molecular target for induced synthetic lethality in cancer cells. *J. Am. Chem. Soc*, **135**, 9640–9643.
47. Wang,Y., Yang,J., Wild,A.T., Wu,W.H., Shah,R., Danussi,C., Riggins,G.J., Kannan,K., Sulman,E.P., Chan,T.A. *et al.* (2019) G-quadruplex DNA drives genomic instability and represents a targetable molecular abnormality in ATRX-deficient malignant glioma. *Nat. Commun*, **10**, 943.
48. Tauchi,T., Shin-ya,K., Sashida,G., Sumi,M., Nakajima,A., Shimamoto,T., Ohyashiki,J.H. and Ohyashiki,K. (2003) Activity of a novel G-quadruplex-interactive telomerase inhibitor, telomestatin (SOT-095), against human leukemia cells: involvement of ATM-dependent DNA damage response pathways. *Oncogene*, **22**, 5338–5347.
49. Biroccio,A., Porru,M., Rizzo,A., Salvati,E., D'Angelo,C., Orlandi,A., Passeri,D., Franceschin,M., Stevens,M.F. and Gilson,E. (2011) DNA damage persistence as determinant of tumor sensitivity to the combination of Topo I inhibitors and telomere-targeting agents. *Clin. Cancer Res*, **17**, 2227–2236.
50. Leonetti,C., Scarsella,M., Riggio,G., Rizzo,A., Salvati,E., D'Incalci,M., Staszewsky,L., Frapolli,R., Stevens,M.F., Stoppacciaro,A. *et al.* (2008) G-quadruplex ligand RHPS4 potentiates the antitumor activity of camptothecins in preclinical models of solid tumors. *Clin. Cancer Res*, **14**, 7284–7291.
51. Zyner,K.G., Mulhearn,D.S., Adhikari,S., Cuesta,S.M., Di Antonio,M., Erard,N., Hannon,G.J., Tannahill,D. and Balasubramanian,S. (2019) Genetic interactions of G-quadruplexes in humans. *eLife*, **8**, e46793.
52. Day,T.A., Layer,J.V., Cleary,J.P., Guha,S., Stevenson,K.E., Tivey,T., Kim,S., Schinzel,A.C., Izzo,F., Doench,J. *et al.* (2017) PARP3 is a promoter of chromosomal rearrangements and limits G4 DNA. *Nat. Commun*, **8**, 15110.
53. del Mundo,I.M., Vasquez,K.M. and Wang,G. (2019) Modulation of DNA structure formation using small molecules. *Biochim. Biophys. Acta - Mol. Cell Res*, **1866**, 118539.
54. Oleksi,A., Blanco,A.G., Boer,R., Usón,I., Aymamí,J., Rodger,A., Hannon,M.J. and Coll,M. (2006) Molecular recognition of a three-way DNA junction by a metallosupramolecular helicate. *Angew. Chem. Int. Ed*, **45**, 1227–1231.
55. Ducani,C., Leczkowska,A., Hodges,N.J. and Hannon,M.J. (2010) Noncovalent DNA-binding metallo-supramolecular cylinders prevent DNA transactions in vitro. *Angew. Chem. Int. Ed*, **49**, 8942–8945.
56. Hotze,A.C., Hodges,N.J., Hayden,R.E., Sanchez-Cano,C., Paines,C., Male,N., Tse,M.-K., Bunce,C.M., Chipman,J.K. and Hannon,M.J. (2008) Supramolecular iron cylinder with unprecedented DNA binding is a potent cytostatic and apoptotic agent without exhibiting genotoxicity. *Chem. Biol*, **15**, 1258–1267.
57. Gómez-González,J., Pérez,Y., Sciortino,G., Roldan-Martín,L., Martínez-Costas,J., Maréchal,J.-D., Alfonso,I., Vázquez López,M. and Vázquez,M.E. (2021) Dynamic stereoselection of peptide helicates and their selective labeling of DNA replication foci in cells. *Angew. Chem. Int. Ed*, **60**, 8859–8866.
58. Zhu,J., Haynes,C.J.E., Kieffer,M., Greenfield,J.L., Greenhalgh,R.D., Nitschke,J.R. and Keyser,U.F. (2019) FeII4L4 tetrahedron binds to nonpaired DNA bases. *J. Am. Chem. Soc*, **141**, 11358–11362.
59. Guyon,L., Pirrotta,M., Duskova,K., Granzhan,A., Teulade-Fichou,M.-P. and Monchaud,D. (2018) TWJ-Screen: an isothermal screening assay to assess ligand/DNA junction interactions in vitro. *Nucleic Acids Res.*, **46**, e16.
60. Duskova,K., Lamarche,J., Amor,S., Caron,C., Queyriaux,N., Gaschard,M., Penouilh,M.-J., de Robillard,G., Delmas,D.,

Devillers,C.H. *et al.* (2019) Identification of three-way DNA junction ligands through screening of chemical libraries and validation by complementary in vitro assays. *J. Med. Chem*, **62**, 4456–4466.
61. Duskova,K., Lejault,P., Benchimol,É., Guillot,R., Britton,S., Granzhan,A. and Monchaud,D. (2020) DNA junction ligands trigger DNA damage and are synthetic lethal with DNA repair inhibitors in cancer cells. *J. Am. Chem. Soc*, **142**, 424–435.
62. Ambrus,A., Chen,D., Dai,J.X., Jones,R.A. and Yang,D.Z. (2005) Solution structure of the biologically relevant g-quadruplex element in the human c-MYC promoter. implications for g-quadruplex stabilization. *Biochem*, **44**, 2048–2058.
63. Chung,W.J., Heddi,B., Hamon,F., Teulade-Fichou,M.P. and Phan,A.T. (2014) Solution structure of a G-quadruplex bound to the bisquinolinium compound Phen-DC3. *Angew. Chem*, **126**, 1017–1020.
64. Thiviyanathan,V., Luxon,B.A., Leontis,N.B., Illangasekare,N., Donne,D.G. and Gorenstein,D.G. (1999) Hybrid-hybrid matrix structural refinement of a DNA three-way junction from 3D NOESY-NOESY. *J. Biomol. NMR*, **14**, 209–221.
65. Amrane,S., De Cian,A., Rosu,F., Kaiser,M., De Pauw,E., Teulade-Fichou,M.-P. and Mergny,J.-L. (2008) Identification of trinucleotide repeat ligands with a FRET melting assay. *ChemBioChem*, **9**, 1229–1234.
66. Novotna,J., Laguerre,A., Granzhan,A., Pirrotta,M., Teulade-Fichou,M.-P. and Monchaud,D. (2015) Cationic azacryptands as selective three-way DNA junction binding agents. *Org. Biomol. Chem*, **13**, 215–222.
67. Granzhan,A., Monchaud,D., Saettel,N., Guédin,A., Mergny,J.-L. and Teulade-Fichou,M.-P. (2010) 'One ring to bind them all'—Part II: identification of promising G-quadruplex ligands by screening of cyclophane-type macrocycles. *J. Nucleic Acids*, **2010**, 460561.
68. Malina,J., Hannon,M.J. and Brabec,V. (2007) Recognition of DNA three-way junctions by metallosupramolecular cylinders: gel electrophoresis studies. *Chem. Eur. J*, **13**, 3871–3877.
69. Chou,T.-C. and Talalay,P. (1984) Quantitative analysis of dose-effect relationships: the combined effects of multiple drugs or enzyme inhibitors. *Adv. Enzyme. Regul.*, **22**, 27–55.
70. Chou,T.-C. (2010) Drug combination studies and their synergy quantification using the Chou-Talalay method. *Cancer Res.*, **70**, 440–446.
71. De Rache,A. and Mergny,J.-L. (2015) Assessment of selectivity of G-quadruplex ligands via an optimised FRET melting assay. *Biochimie*, **115**, 194–202.
72. Haudecoeur,R., Stefan,L. and Monchaud,D. (2013) Multitasking water-soluble synthetic G-quartets: from preferential RNA-quadruplex interaction to biocatalytic activity. *Chem. Eur. J*, **19**, 12739–12747.
73. Ragazzon,P.A., Garbett,N.C. and Chaires,J.B. (2007) Competition dialysis: a method for the study of structural selective nucleic acid binding. *Methods*, **42**, 173–182.
74. Lin,C., Dickerhoff,J. and Yang,D. (2019) NMR studies of G-quadruplex structures and G-quadruplex-interactive compounds. In: *G-Quadruplex Nucleic Acids*. Springer, pp. 157–176.
75. Haider,S.M., Neidle,S. and Parkinson,G.N. (2011) A structural analysis of G-quadruplex/ligand interactions. *Biochimie*, **93**, 1239–1251.
76. Ropp,P.J., Spiegel,J.O., Walker,J.L., Green,H., Morales,G.A., Milliken,K.A., Ringe,J.J. and Durrant,J.D. (2019) Gypsum-DL: an open-source program for preparing small-molecule libraries for structure-based virtual screening. *J. Cheminformatics*, **11**, 34.
77. Morris,G.M., Huey,R., Lindstrom,W., Sanner,M.F., Belew,R.K., Goodsell,D.S. and Olson,A.J. (2009) AutoDock4 and AutoDockTools4: automated docking with selective receptor flexibility. *J. Comput. Chem*, **30**, 2785–2791.
78. Hess,B., Kutzner,C., van der Spoel,D. and Lindahl,E. (2008) GROMACS 4: algorithms for highly efficient, load-balanced, and scalable molecular simulation. *J. Chem. Theory Comput.*, **4**, 435–447.
79. Pronk,S., Páll,S., Schulz,R., Larsson,P., Bjelkmar,P., Apostolov,R., Shirts,M.R., Smith,J.C., Kasson,P.M., van der Spoel,D. *et al.* (2013) GROMACS 4.5: a high-throughput and highly parallel open source molecular simulation toolkit. *Bioinformatics*, **29**, 845–854.
80. Páll,S., Abraham,M.J., Kutzner,C., Hess,B. and Lindahl,E. (2014) In: *Tackling Exascale Software Challenges in Molecular Dynamics Simulations with GROMACS*. International Conference on Exascale Applications and Software, Springer, pp. 3–27.
81. Abraham,M.J., Murtola,T., Schulz,R., Páll,S., Smith,J.C., Hess,B. and Lindahl,E. (2015) GROMACS: High performance molecular simulations through multi-level parallelism from laptops to supercomputers. *SoftwareX*, **1-2**, 19–25.
82. Jourdan,M., Garcia,J., Lhomme,J., Teulade-Fichou,M.-P., Vigneron,J.-P. and Lehn,J.-M. (1999) Threading bis-intercalation of a macrocyclic bisacridine at Abasic sites in DNA: nuclear magnetic resonance and molecular modeling study. *Biochem*, **38**, 14205–14213.
83. Cudic,P., Vigneron,J.-P., Lehn,J.-M., Cesario,M. and Prangé,T. (1999) Molecular recognition of azobenzene dicarboxylates by acridine-based receptor molecules, crystal structure of the supramolecular inclusion complex of trans-3,3′-azobenzene dicarboxylate with a cyclo-bis-intercaland receptor. *Eur. J. Org. Chem*, **1999**, 2479–2484.
84. Jourdan,M., Granzhan,A., Guillot,R., Dumy,P. and Teulade-Fichou,M.-P. (2012) Double threading through DNA: NMR structural study of a bis-naphthalene macrocycle bound to a thymine–thymine mismatch. *Nucleic. Acids. Res.*, **40**, 5115–5128.
85. Amendola,V., Bergamaschi,G. and Miljkovic,A. (2018) Azacryptands as molecular cages for anions and metal ions. *Supramol. Chem.*, **30**, 236–242.
86. La Cognata,S., Miljkovic,A., Mobili,R., Bergamaschi,G. and Amendola,V. (2020) Organic cages as building blocks for mechanically interlocked molecules: towards molecular machines. *ChemPlusChem*, **85**, 1145–1155.
87. Alibrandi,G., Amendola,V., Bergamaschi,G., Fabbrizzi,L. and Licchelli,M. (2015) Bistren cryptands and cryptates: versatile receptors for anion inclusion and recognition in water. *Org. Biomol. Chem*, **13**, 3510–3524.
88. Soule,H., Vazquez,J., Long,A., Albert,S. and Brennan,M. (1973) A human cell line from a pleural effusion derived from a breast carcinoma. *J. Natl. Cancer Inst.*, **51**, 1409–1416.
89. Levenson,A.S. and Jordan,V.C. (1997) MCF-7: the first hormone-responsive breast cancer cell line. *Cancer Res.*, **57**, 3071–3078.
90. Cailleau,R., Young,R., Olive,M. and Reeves,W. Jr (1974) Breast tumor cell lines from pleural effusions. *J. Natl. Cancer Inst.*, **53**, 661–674.
91. Skehan,P., Storeng,R., Scudiero,D., Monks,A., McMahon,J., Vistica,D., Warren,J.T., Bokesch,H., Kenney,S. and Boyd,M.R. (1990) New colorimetric cytotoxicity assay for anticancer-drug screening. *J. Natl. Cancer Inst*, **82**, 1107–1112.
92. Vichai,V. and Kirtikara,K. (2006) Sulforhodamine B colorimetric assay for cytotoxicity screening. *Nat. Protoc*, **1**, 1112.
93. Bonner,W.M., Redon,C.E., Dickey,J.S., Nakamura,A.J., Sedelnikova,O.A., Solier,S. and Pommier,Y. (2008) γH2AX and cancer. *Nat. Rev. Cancer*, **8**, 957.
94. Burma,S., Chen,B.P., Murphy,M., Kurimasa,A. and Chen,D.J. (2001) ATM phosphorylates histone H2AX in response to DNA double-strand breaks. *J. Biol. Chem*, **276**, 42462–42467.
95. Paull,K., Shoemaker,R., Hodes,L., Monks,A., Scudiero,D., Rubinstein,L., Plowman,J. and Boyd,M. (1989) Display and analysis of patterns of differential activity of drugs against human tumor cell lines: development of mean graph and COMPARE algorithm. *J. Natl. Cancer Inst*, **81**, 1088–1092.
96. Shoemaker,R.H. (2006) The NCI60 human tumour cell line anticancer drug screen. *Nat. Rev. Cancer*, **6**, 813–823.
97. Hampel,S.M., Pepe,A., Greulich-Bode,K.M., Malhotra,S.V., Reszka,A.P., Veith,S., Boukamp,P. and Neidle,S. (2013) Mechanism of the antiproliferative activity of some naphthalene diimide G-quadruplex ligands. *Mol. Pharmacol*, **83**, 470–480.
98. Saleh,M.M., Laughton,C.A., Bradshaw,T.D. and Moody,C.J. (2017) Development of a series of bis-triazoles as G-quadruplex ligands. *RSC Adv.*, **7**, 47297–47308.
99. Larsen,A.K., Grondard,L., Couprie,J., Desoize,B., Comoe,L., Jardillier,J.-C. and Riou,J.-F. (1993) The antileukemic alkaloid fagaronine is an inhibitor of DNA topoisomerases I and II. *Biochem. Pharmacol*, **46**, 1403–1412.
100. Olivieri,M., Cho,T., Álvarez-Quilón,A., Li,K., Schellenberg,M.J., Zimmermann,M., Hustedt,N., Rossi,S.E., Adam,S., Melo,H. *et al.*

(2020) A genetic map of the response to DNA damage in human cells. *Cell*, **182**, 481–496.
101. Bruno,P.M., Lu,M., Dennis,K.A., Inam,H., Moore,C.J., Sheehe,J., Elledge,S.J., Hemann,M.T. and Pritchard,J.R. (2020) The primary mechanism of cytotoxicity of the chemotherapeutic agent CX-5461 is topoisomerase II poisoning. *Proc. Natl. Acad. Sci. U.S.A*, **117**, 4053–4060.
102. Bossaert,M., Pipier,A., Riou,J.F., Noirot,C., Nguyễn,L.-T., Serre,R.-F., Bouchez,O., Defrancq,E., Calsou,P., Britton,S. *et al.* (2021) Transcription-associated topoisomerase activities control DNA-breaks production by G-quadruplex ligands. *eLife*, **10**, e65184.
103. Kawatani,M., Takayama,H., Muroi,M., Kimura,S., Maekawa,T. and Osada,H. (2011) Identification of a small-molecule inhibitor of DNA topoisomerase II by proteomic profiling. *Chem. Biol*, **18**, 743–751.
104. Jensen,P.B. and Sehested,M. (1997) DNA topoisomerase II rescue by catalytic inhibitors: a new strategy to improve the antitumor selectivity of etoposide. *Biochem. Pharmacol*, **54**, 755–759.
105. Treangen,T.J. and Salzberg,S.L. (2012) Repetitive DNA and next-generation sequencing: computational challenges and solutions. *Nat. Rev. Genet*, **13**, 36–46.
106. Cañeque,T., Müller,S. and Rodriguez,R. (2018) Visualizing biologically active small molecules in cells using click chemistry. *Nat. Rev. Chem*, **2**, 202–215.
107. Biffi,G., Tannahill,D., McCafferty,J. and Balasubramanian,S. (2013) Quantitative visualization of DNA G-quadruplex structures in human cells. *Nat. Chem*, **5**, 182–186.
108. Britton,S., Coates,J. and Jackson,S.P. (2013) A new method for high-resolution imaging of Ku foci to decipher mechanisms of DNA double-strand break repair. *J. Cell Biol*, **202**, 579–595.
109. Koningsbruggen,S.V., Gierliński,M., Schofield,P., Martin,D., Barton,G.J., Ariyurek,Y., Dunnen,J.T. and Lamond,A.I. (2010) High-resolution whole-genome sequencing reveals that specific chromatin domains from most human chromosomes associate with nucleoli. *Mol. Biol. Cell*, **21**, 3735–3748.
110. Németh,A., Conesa,A., Santoyo-Lopez,J., Medina,I., Montaner,D., Péterfia,B., Solovei,I., Cremer,T., Dopazo,J. and Längst,G. (2010) Initial genomics of the human nucleolus. *PLoS Genet.*, **6**, e1000889.
111. Bizhanova,A. and Kaufman,P.D. (2021) Close to the edge: heterochromatin at the nucleolar and nuclear peripheries. *Biochim. Biophys. Acta (BBA) - Gene Regul. Mech.*, **1864**, 194666.
112. Caburet,S., Conti,C., Schurra,C., Lebofsky,R., Edelstein,S.J. and Bensimon,A. (2005) Human ribosomal RNA gene arrays display a broad range of palindromic structures. *Genome Res.*, **15**, 1079–1085.
113. Wang,J.C. (2002) Cellular roles of DNA topoisomerases: a molecular perspective. *Nat. Rev. Mol. Cell Biol*, **3**, 430–440.
114. Wang,G. and Vasquez,K.M. (2006) Non-B DNA structure-induced genetic instability. *Mutat. Res*, **598**, 103–119.
115. Vasquez,K.M. and Wang,G. (2013) The yin and yang of repair mechanisms in DNA structure-induced genetic instability. *Mut. Res.-Fundam. Mol. Mech. Mutagen.*, **743**, 118–131.
116. Froelich-Ammon,S., Gale,K.C. and Osheroff,N. (1994) Site-specific cleavage of a DNA hairpin by topoisomerase II. DNA secondary structure as a determinant of enzyme recognition/cleavage. *J. Biol. Chem*, **269**, 7719–7725.
117. Jonstrup,A.T., Thomsen,T., Wang,Y., Knudsen,B.R., Koch,J. and Andersen,A.H. (2008) Hairpin structures formed by alpha satellite DNA of human centromeres are cleaved by human topoisomerase IIα. *Nucleic Acids Res.*, **36**, 6165–6174.
118. Atkin,N.D., Raimer,H.M. and Wang,Y.-H. (2019) Broken by the cut: a journey into the role of topoisomerase II in DNA fragility. *Genes*, **10**, 791.
119. Szlachta,K., Manukyan,A., Raimer,H.M., Singh,S., Salamon,A., Guo,W., Lobachev,K.S. and Wang,Y.-H. (2020) Topoisomerase II contributes to DNA secondary structure-mediated double-stranded breaks. *Nucleic Acids Res.*, **48**, 6654–6671.
120. Nitiss,J.L. (2009) Targeting DNA topoisomerase II in cancer chemotherapy. *Nat. Rev. Cancer*, **9**, 338–350.
121. Delgado,J.L., Hsieh,C.-M., Chan,N.-L. and Hiasa,H. (2018) Topoisomerases as anticancer targets. *Biochem. J*, **475**, 373–398.
122. Pilati,P., Nitti,D. and Mocellin,S. (2012) Cancer resistance to type II topoisomerase inhibitors. *Curr. Med. Chem*, **19**, 3900–3906.
123. Peltonen,K., Colis,L., Liu,H., Trivedi,R., Moubarek,M.S., Moore,H.M., Bai,B., Rudek,M.A., Bieberich,C.J. and Laiho,M. (2014) A targeting modality for destruction of RNA polymerase I that possesses anticancer activity. *Cancer Cell*, **25**, 77–90.
124. Chodosh,L.A., Fire,A., Samuels,M. and Sharp,P.A. (1989) 5,6-Dichloro-1-β-D-ribofuranosylbenzimidazole inhibits transcription elongation by RNA polymerase II in vitro. *J. Biol. Chem*, **264**, 2250–2257.
125. Spadari,S., Sala,F. and Pedrali-Noy,G. (1982) Aphidicolin: a specific inhibitor of nuclear DNA replication in eukaryotes. *Trends Biochem. Sci*, **7**, 29–32.
126. Leonard,C.J. and Berns,K.I. (1994) Adeno-associated virus type 2: a latent life cycle In: Cohn, W.E. and Moldave,K. (eds). *Progress in Nucleic Acid Research and Molecular Biology*. Academic Press, Vol. **48**, pp. 29–52.
127. Berns,K.I. (2020) The unusual properties of the AAV inverted terminal repeat. *Hum. Gene Ther*, **31**, 518–523.
128. Shaheen,M., Allen,C., Nickoloff,J.A. and Hromas,R. (2011) Synthetic lethality: exploiting the addiction of cancer to DNA repair. *Blood*, **117**, 6074–6082.
129. Leahy,J.J., Golding,B.T., Griffin,R.J., Hardcastle,I.R., Richardson,C., Rigoreau,L. and Smith,G.C. (2004) Identification of a highly potent and selective DNA-dependent protein kinase (DNA-PK) inhibitor (NU7441) by screening of chromenone libraries. *Bioorg. Med. Chem. Lett*, **14**, 6083–6087.
130. Hickson,I., Zhao,Y., Richardson,C.J., Green,S.J., Martin,N.M., Orr,A.I., Reaper,P.M., Jackson,S.P., Curtin,N.J. and Smith,G.C. (2004) Identification and characterization of a novel and specific inhibitor of the ataxia-telangiectasia mutated kinase ATM. *Cancer Res.*, **64**, 9152–9159.
131. Huang,F., Motlekar,N.A., Burgwin,C.M., Napper,A.D., Diamond,S.L. and Mazin,A.V. (2011) Identification of specific inhibitors of human RAD51 recombinase using high-throughput screening. *ACS Chem. Biol*, **6**, 628–635.
132. Tang,J., Wennerberg,K. and Aittokallio,T. (2015) What is synergy? The Saariselkä agreement revisited. *Front. Pharmacol.*, **6**, 181.
133. Rodriguez,R., Mueller,S., Yeoman,J.A., Trentesaux,C., Riou,J.-F. and Balasubramanian,S. (2008) A novel small molecule that alters shelterin integrity and triggers a DNA-damage response at telomeres. *J. Am. Chem. Soc*, **130**, 15758–15758.
134. De Cian,A., DeLemos,E., Mergny,J.-L., Teulade-Fichou,M.-P. and Monchaud,D. (2007) Highly efficient G-quadruplex recognition by bisquinolinium compounds. *J. Am. Chem. Soc*, **129**, 1856–1857.
135. De Cian,A., Cristofari,G., Reichenbach,P., De Lemos,E., Monchaud,D., Teulade-Fichou,M.-P., Shin-Ya,K., Lacroix,L., Lingner,J. and Mergny,J.-L. (2007) Reevaluation of telomerase inhibition by quadruplex ligands and their mechanisms of action. *Proc. Natl. Acad. Sci. U.S.A*, **104**, 17347–17352.
136. Pennarun,G., Granotier,C., Gauthier,L.R., Gomez,D. and Boussin,F.D. (2005) Apoptosis related to telomere instability and cell cycle alterations in human glioma cells treated by new highly selective G-quadruplex ligands. *Oncogene*, **24**, 2917–2928.
137. Granotier,C., Pennarun,G., Riou,L., Hoffschir,F., Gauthier,L.R., De Cian,A., Gomez,D., Mandine,E., Riou,J.F., Mergny,J.L. *et al.* (2005) Preferential binding of a G-quadruplex ligand to human chromosome ends. *Nucleic Acids Res.*, **33**, 4182–4190.